Sustainable Chemical Engineering
http://ojs.wiserpub.com/index.php/SCE/

Research Article

A New Fe_2O_3-Graphene-Hydrazine Sulphate Nanocomposite as Anode Material with Enhanced Electrocatalytic Activity in an H_2O_2 Fuel Cell

Madhavi D. Shete*, J. B. Fernandes

Department of Chemistry, Goa University, Taleigao, Goa 403206, India
Email: smadhavi91@gmail.com

Received: 10 October 2023; **Revised:** 8 November 2023; **Accepted:** 14 November 2023

Abstract: In the present study, synthesis of various phases of iron oxide was carried out by simple combustion method. The synthesized iron oxides and their composites with graphene and hydrazine sulphate are investigated as electrocatalytic materials for hydrogen peroxide (H_2O_2) fuel cells. The activity was seen to be dependent on the phase composition, surface features and electrical properties which was altered due to the use of the different amount of oxalic acid as one of the precursors during the synthesis. The catalysts which are more active for decomposition of hydrogen peroxide, showed lower electrocatalytic activity. A significantly improved electrocatalytic performance is obtained when a nanocomposite electrocatalyst is prepared using iron oxide, graphene and hydrazine sulphate.

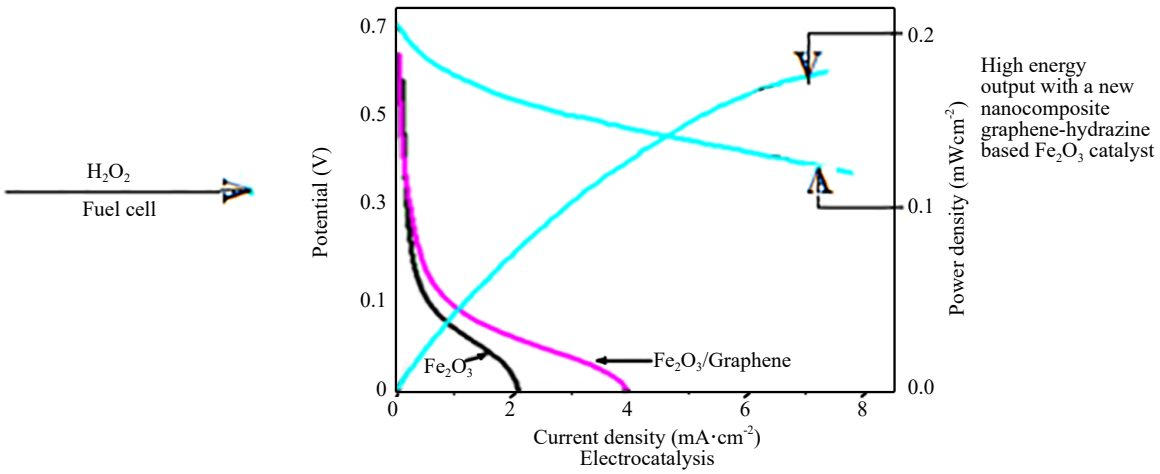

Keywords: iron oxide, tafel polarization, electrocatalyst, H_2O_2, fuel cell

DOI: https://doi.org/10.37256/sce.5120243756

1. Introduction

In fuel cells, the energy of a chemical reaction is converted to electricity. The major challenge is to carry out efficient oxidation of the fuel, by using suitable electrocatalysts. Apart from the noble metal catalysts, metal oxides have also been extensively investigated in fuel cells.[1-5] Different types of fuel cells and their working is discussed by M. Schulze et al.[6] S. Wasmus et al. reported the fundamental characteristics of catalyst study and their use in the methanol oxidation and direct methanol oxidation fuel cell.[7] The study of the microbial fuel cells is introduced by M. Rahimnejad for bioelectricity generation.[8] H. Firouzjaie et al. discussed their work catalytic advantages, challenges and priorities in alkaline membrane fuel cells.[9] A study of molten carbonate fuel cells for generation of the high ash Indian coal is being reported by R. Perumal et al.[10] Metal oxide solid oxide fuel cell is being reported by S. Opakhai et al.[11] O. Zerbinati et al. reported a direct methanol fuel cell using black platinum as the electrocatalyst[12] H_2O_2 fuel cell is recently in focus as a one-compartment fuel cell in which H_2O_2 is used both as a fuel as well as an oxidant.[13-18] A theoretical voltage of 1.09 volts is expected for the H_2O_2 fuel cell. Hydrogen peroxide fuel cell has been investigated by using different metals as cathode and anode. In the beginning, an H_2O_2 fuel cell was introduced by using an Au plate as an anode and an Ag plate as a cathode and an open circuit potential (OCP) of 0.2 V was obtained.[19] Later iron phthalocyanine complex or Prussian blue were used as cathode materials and an improved OCP of around 0.55 V was obtained.[20-21] However, when $Fe_3[Co(CN)_6]_2$ as anode and Ni mesh as cathode were used, an OCP of 0.8 V was generated.[20]

Metal oxides have so far not been used in H_2O_2 fuel cell electrocatalysis although several metal oxides are considered as useful electrocatalytic materials in other fuel cells such as the direct methanol fuel cells etc.[21] CeO_2/rGO/Pt nanostructured metal oxide electrocatalyst reported for its function in the anodic methanol oxidation of direct methanol fuel cells due to its rigid metallic structure and high electronic conductivity of the reduced graphene oxide. Similarly, $CaTiO_{3-\delta}$ was also reported for its use in the oxygen reduction reaction in direct methanol fuel cells which is due to the presence of oxygen vacancies as available active sites for oxygen adsorption in the lattice. Ceria (CeO_2) as a co-catalytic material with Pt, has been also reported. Wherein it was explained that the presence of biocatalysts and their low-cost use in methanol electrooxidation reaction.[22-23] The main reason for this is probably the high reactivity of metal oxides which can cause rapid nonelectrochemical decomposition of hydrogen peroxide. This would result in waste of the H_2O_2 both as a fuel as well as an oxidant. Iron oxides can be considered as one of the alternatives to use as catalysts in H_2O_2 fuel cell as it is low cost, thermodynamically stable, affords facile synthesis, and also has its natural abundance and is well explained by N Chengsheng et al.[24] However, as iron oxides have the ability to decompose H_2O_2 very easily, it may not be generally considered as an active material for its use in H_2O_2 electrocatalysis. This can discourage the use of iron oxides which are materials that can be economically exploited and easily synthesized. It is nevertheless important to note that the reactivity of iron oxides like most transition metal oxides, would be greatly influenced by the method used in their synthesis.[25] Several types of iron oxides can be readily synthesized in the laboratory. There exist several polymorphs of ferric oxide such as hematite or maghemite also referred to as α-Fe_2O_3 or γ-Fe_2O_3. In the present investigation, attention is given to carry out the synthesis of various phases of iron oxides for their application in H_2O_2 fuel cells as anode material. Synthesised iron oxide shows promising electrocatalytic activity. A significant improvement in the performance of the H_2O_2 fuel cell was obtained by synthesising graphene-supported iron oxide-hydrazine sulphate nanocomposite.

2. Experimental

2.1 *Synthesis of α-Fe_2O_3*

All the chemicals used were of analytical grade. Ferric nitrate, oxalic acid and urea were mixed together such that the respective ratios of ferric nitrate: urea: oxalic acid were 1:2:*x*, where *x* = 1, 2, 3, 5 various molar ratios of oxalic acid with respect to ferric nitrate and urea. The mixture was preheated uniformly up to 60 °C. The resulting yellowish-green colored residue was heated in a furnace at 400 °C for 2 h to obtain the final stable samples. The synthesized iron oxide samples were designated as F-121, F-122, F-123, F-125.

Synthesis of graphene oxide (GO) was carried out by an improved Hummer's method,[26] which was later combined with iron oxide to give a graphene iron oxide composite as discussed in section 2.2.

2.2 *Synthesis of Fe_2O_3/graphene composite*

15 mg of GO was dispersed in 20 mL of distilled water by sonication. 600 mg of F-125 was added to the GO dispersion and the resulting mixture was stirred for 2 h. It was dried at 60 °C and followed by calcination at 200 °C. This gave a composite of 2.5% graphene with an F-125 catalyst. It was designated as F-125/2.5 G. [Note: sample of iron oxide F-125 was selected as one of the active materials to synthesis composite with the graphene-based on the high electrocatalytic activity of F-125 in H_2O_2 fuel cell].

2.3 *Synthesis of Fe_2O_3/graphene/hydrazine sulphate composite*

An iron oxide graphene composite F-125/4.5 G was prepared by mixing 0.5 g of F-125 with graphene oxide. Here 4.5 represents % GO in the composite. 5 mL of 1 M hydrazine sulphate was then added to the composite, with constant stirring. The product was dried at 60 °C in an oven for 2 h. It was designated as F-125/4.5 G/$HySO_4$ where hydrazine sulphate ($N_2H_4.H_2SO_4$), for convenience is written as $HySO_4$.

2.4 *Characterization*

Phase identification was carried out by X-ray diffractions (XRD) analysis using Cu Kα radiation (λ = 1.5406 Å) and the lattice parameters were calculated from the 'd' values. IR spectra were recorded using KBr. The Brunauer-Emmett-Teller (BET) surface area was determined by a multipoint BET method. The particle sizes were determined by Transmission electron microscopy (TEM) analysis. Electrical properties were studied by using high frequency LCR bridge meters 6,500 p series using Wayne software at series circuit. The dielectric constant was further calculated by using capacitance values and substituting in the equation (ε') = $C_p t/\varepsilon_o A$. where C_p is the capacitance, t is the thickness of the pallet used, A is the cross-section area of the pallet, and ε_o is the permittivity of free space (8.854×10^{-12} F/m). Ac conductivity is calculated by using $\sigma_{ac} = \omega\varepsilon'\varepsilon_o$ tanδ. where ω is the angular frequency and tanδ is the D factor values obtained directly. Impedance is calculated by using the equation $\sqrt{R^2 + X^2}$. Where R is the resistance and X is the reactance values obtained after measurement. The band gap energies were determined by UV-VIS spectrophotometry by plotting a graph of $(ah\upsilon)^2$ Vs $h\upsilon$. Where 'a' is the absorbance values obtained, 'h' is the Planck's constant and $\upsilon = c/\lambda$. Therefore one can get direct values of the band gap from the respective plots. Another method employed to obtain band gap was cyclic voltammetry by using a three-electrodes assembly with Pt wire as the counter electrode and Ag/Ag^+ as a reference electrode. The working electrodes were prepared by coating the catalyst on a glassy carbon (GCE). The electrolyte was 100 mm of tetrabutylammonium perchlorate in acetonitrile. Prior to the CV measurements, the GCE electrode was first activated by scanning in the potential range +1.0 to -1.0 V in a freshly prepared 1 M H_2SO_4.[27-28]

2.5 *Catalytic tests*

(i) Decomposition of H_2O_2.

The catalytic decomposition of H_2O_2 was carried out on 10 mg of catalyst containing 5 mL of 0.1 M H_2O_2 (pH 5) and measuring the evolved oxygen gas at various time intervals. The reactions were carried out in the dark as well as by exposing the reaction mixture to sunlight.

(ii) Electrode preparation.

Cleaning and activation of glassy carbon electrode (GCE) electrode: Polish GCE electrode with 0.05 mm alumina slurry and then chemically cleaned and activated by repeated cycle potential scanning within potential range +1 to -1 in freshly prepared 1 M H_2SO_4 then wash it and coat with material and use.

The electrode of iron oxide nanoparticles was prepared by casting electrolyte ink on the glassy carbon electrode. The electrocatalyst ink was prepared by dispersing 2 mg of iron oxide electrocatalyst in 0.2 mL of Nafion mixture. The dispersion was sonicated for 30 min to form homogenous ink. Next 4 µL of electrolyte ink was deposited on GCE and dried in air at room temperature.

(iii) Testing of the synthesized iron oxide catalyst and its composites.

The electrocatalytic activity was carried out in a one-compartment H_2O_2 fuel cell setup. OCP was determined by using Ag wire and GCE. GCE was coated with the catalyst film. The electrolyte was a 1:1 (v/v) mixture of 1 M H_2O_2 +

1 M NaCl at pH = 1. Tafel polarization measurements were carried out by using Pt wire as a counter electrode and Ag/Ag^+ as a reference electrode.[26]

3 Results and discussion

3.1 *Synthesis and characterization*

Figure 1 gives the XRD patterns of the synthesized Fe_2O_3 samples.

In the case of F-121 and F-122, all the peaks were due to α-Fe_2O_3 (hematite). However, F-123 was pure γ phase (maghemite, JCPDS file: 33-0664). F-125 was mainly hematite with some peaks due to the maghemite phase (peaks at around 30 °C and 42 °C). It is clear from the XRD patterns of F-122 and F-123 that phase change from hematite to maghemite occurred due to excess use of oxalic acid (3 moles). However, when oxalic acid used was in a large excess (5 moles) as in the case of F-125, there was increased exothermicity during synthesis. This resulted in the reappearance of some peaks due to hematite. Thus F-125 was a mixed phase oxide containing peaks due to both alpha and gamma phases.

The lattice prameters obtained from XRD analysis along with TEM particle sizes (Figure 2) and band gap values are presented in Table 1.

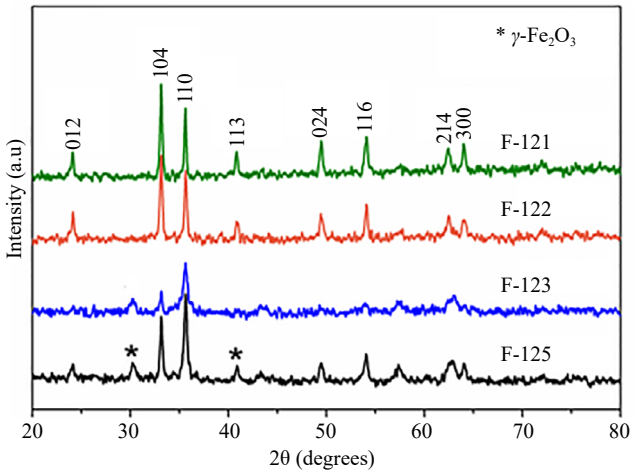

Figure 1. XRD patterns of Fe_2O_3 samples. F-121 and F-122 belong to α-Fe_2O_3 phase while F-123 is γ phase. F-125 is (α, γ) mixed phase
* represents peaks due to γ phase

Table 1. Synthesis of iron oxides and their structural parameters

Catalyst code	Urea m	Oxalicacid n	Phase	Lattice parameters a = b	c	Particle size (nm) TEM	Oxidation potential (E^{onset}ox)	Reduction potential (E^{onset}red)	Band gap from CV (eV)	Band gap from UV (eV)
F-121	2	1	α-Fe_2O_3	5.036	13.78	16	-0.369	1.385	1.754	1.83
F-122	2	2	α-Fe_2O_3	5.033	13.84	13	-0.434	1.449	1.885	1.84
F-123	2	3	γ-Fe_2O_3	Cubic a = 8.349		8	-0.891	1.264	2.155	2.06
F-125	2	5	(α + γ)-Fe_2O_3	Cubic a = 8.202		10	-1.142	1.406	2.548	1.94

m & n represent moles of urea and oxalic acid respectively, per mole of ferric nitrate used during synthesis

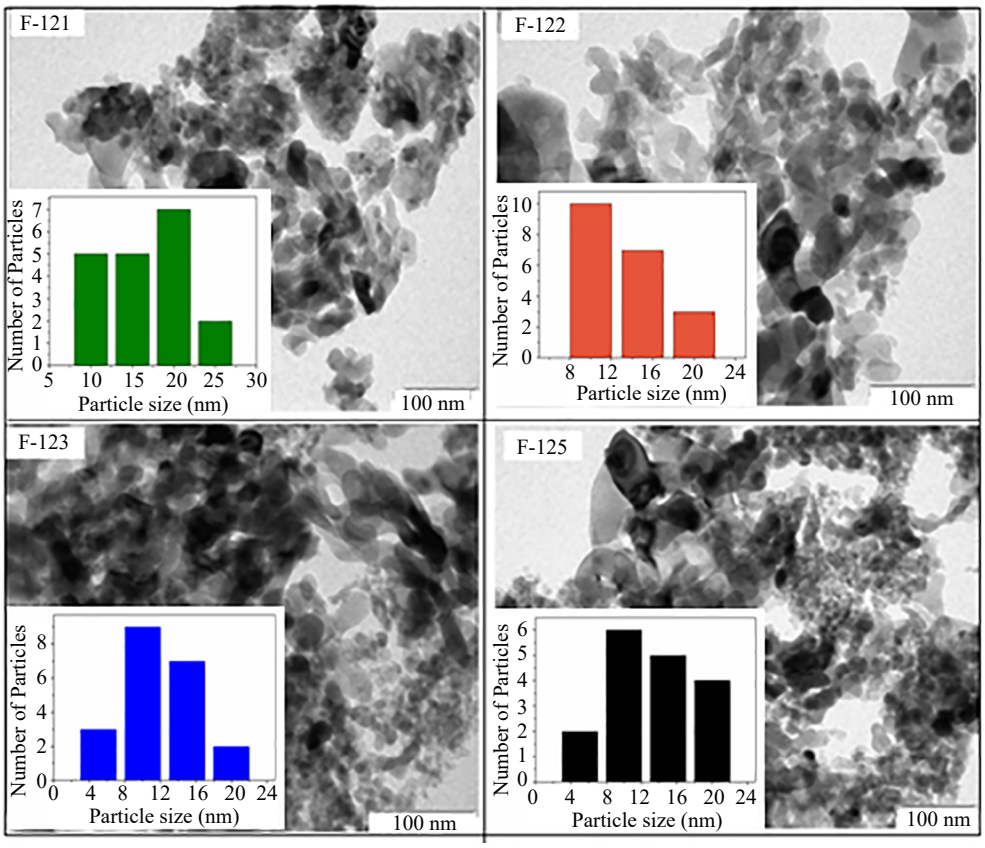

Figure 2. TEM images of the various synthesized iron oxide samples

It can be seen that the particle sizes of the synthesised iron oxide were in the range of 8-16 nm. The samples having γ phase showed lower particle sizes around 8 nm. Figure 3 is the UV-Vis analysis of the synthesized iron oxides. The band gap of the samples was determined by plotting graph $(ah\upsilon)^2$ Vs $h\upsilon$.

The band gap values of all the samples were generally between 1.8 to 2.5 eV. Figure 3(b) Cyclic voltammogram of iron oxides modified GCE. The band edges can be calculated from the onset oxidation potential (E_{oxi}) and onset reduction potential (E_{red}) according to the following equation.

$$E^{edge}_{CB} = -Ip = -(E_{oxi} + 4.71)\ eV$$

$$E^{edge}_{VB} = -Ea = -(E_{red} + 4.71)\ eV$$

where Ip is an ionization potential correlated to E_{oxi} and Ea is the electron affinity corresponding with E_{red}.

The surface area and porosity data are presented in Table 2 along with electrical properties.

Table 2. Surface area and electrical properties of the samples

Catalyst	Phase	Surface area (m^2/g)	Pore volume(cc/g)	Pore radii (Å)	Dielectric constant at 1MHz	Tangent loss at 1MHz	Impedance (Ohm) × 10^9	ac Conductivity at 1MHz (S/cm) × 10^{-7}
F-121	α-Fe_2O_3	7.77	0.033	62.3	10.4	0.08	2.15	4.78
F-122	α-Fe_2O_3	20.56	0.095	72.4	7.5	0.02	4.61	1.17
F-123	γ-Fe_2O_3	32.35	0.194	107.7	9.2	0.04	3.38	2.08
F-125	($\alpha + \gamma$)-Fe_2O_3	42.08	0.282	106.7	13.0	0.04	3.21	3.46

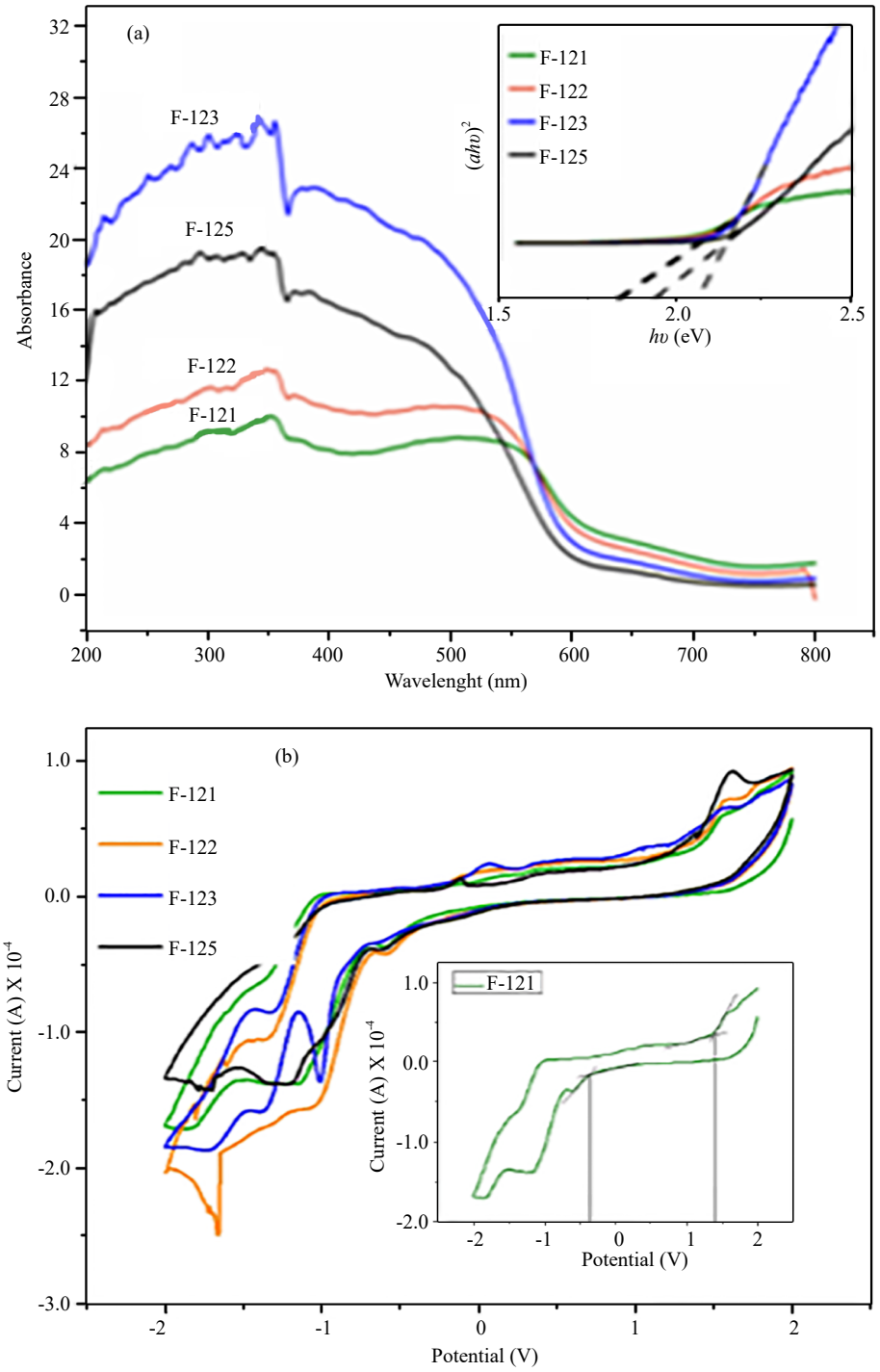

Figure 3. (a) UV-Vis profiles for the synthesised iron oxide (b) Determination of band gap energies of the iron oxide samples using the cyclic voltammetry technique.[18] The cyclic voltamograms were recorded in 100 mM TBAP at 100 mV/s scan rate

It is seen from Table 2 and Figure 4, that the samples with γ phase F-123 and $\alpha + \gamma$ phase of F-125 which had lower particle sizes showed much larger surface areas as compared to the α phase samples F-121 and F-122. The former also showed larger pore radii and pore volume. Thus, the pore volume of F-125 which was prepared using 5 moles of oxalic acid was 0.28 cm^3 as compared to F-121 where the pore volume was merely 0.033 cm^3. Thus, excess use of oxalic acid helped in obtaining oxides with decreased particle size, high surface area and larger pore volume.

Table 1 Lattice strain in the synthesized iron oxide wes determined using Williamson-Hall plots.[29] The respective lattice strain values for F-121, F-122, F-123, and F-125 are -0.25, 0.125, 0.240, 0.125. Higher lattice strain (0.240) is observed in the case of F-123 which was pure γ-Fe_2O_3 as compared to other synthesized iron oxides. A negative value of the lattice strain is due to lattice compression and the positive value is due to lattice expansion.[30-31] IR vibrations obtained in the region 400-1,000 cm^{-1} were due to Fe-O bonds as seen in Figure 5.[29] The vibrational bands between 1,200 and 1,600 cm^{-1} are attributed to the solid state defects or lattice imperfections, which generally arise in the samples prepared by the combustion method. Band between 3,500 and 1,600 cm^{-1} is due to OH stretching and bending absorptions.[31-32]

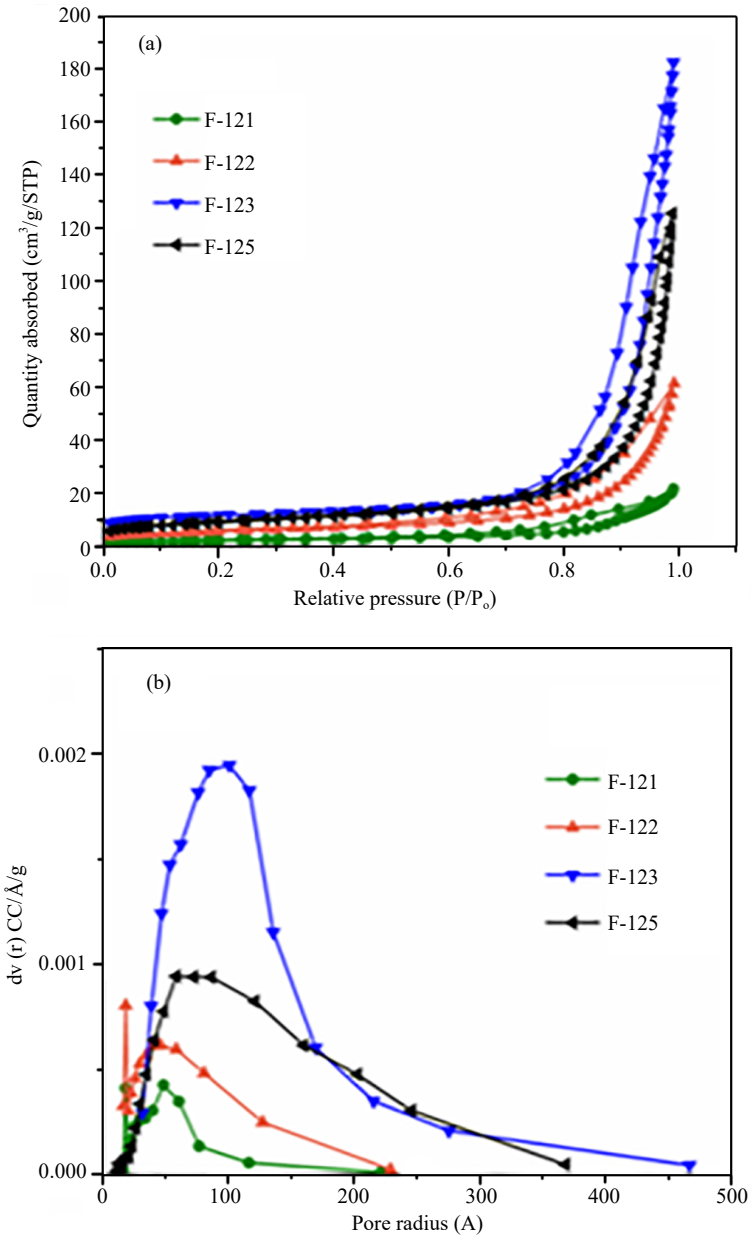

Figure 4. (a) N_2 adsorption-desorption isotherms for synthesized iron oxide catalysts. (b) BJH pore size distribution profiles

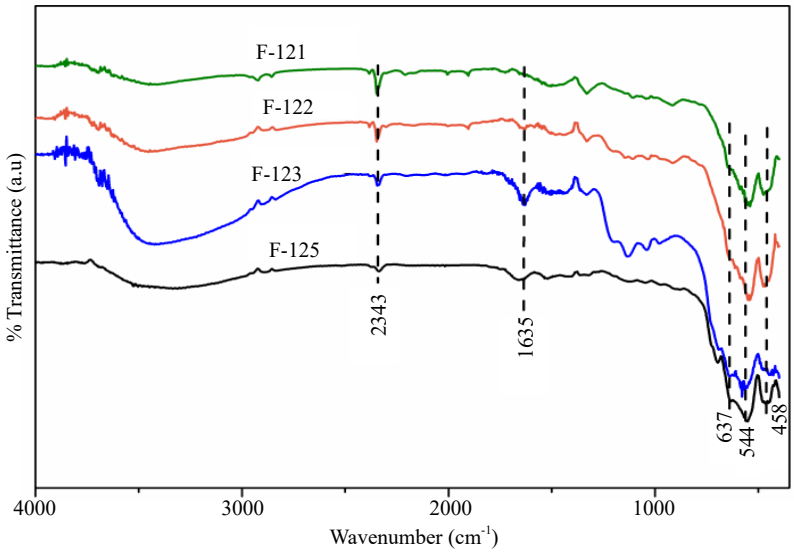

Figure 5. IR spectra of the synthesized iron oxides

3.2 *Catalytic activity for decomposition of H_2O_2 in relation to H_2O_2 fuel cell*

In H_2O_2 fuel cell, the following reactions occur

$$\text{Anode: } H_2O_2 \rightarrow O_2 + 2H^+ + 2e^- \quad E^o = 0.68 \text{ V} \tag{1}$$

$$\text{Cathode: } H_2O_2 + 2H^+ + 2e^- \rightarrow 2H_2O \quad E^o = 1.77 \text{ V} \tag{2}$$

$$\text{Net reaction: } 2H_2O_2 \rightarrow O_2 + 2H_2O \quad E^o_{cell} = 1.09 \text{ V} \tag{3}$$

The fuel cell energy is produced by the anodic oxidation of hydrogen peroxide and its reduction at the cathode. Therefore for fuel cell efficiency, it is important in such processes that H_2O_2 will not undergo nonelectrochemical decomposition in the presence of a catalyst. However, H_2O_2 is known to undergo heterogeneous catalytic decomposition (nonelectrochemical) i.e. without electron transfer at the electrode-electrolyte interface on various transition metal oxides. It is therefore desirable to choose an appropriate iron oxide that would have minimum catalytic activity to liberate O_2. Figure 6 gives H_2O_2 decomposition profiles.

The decomposition occurs as per the reaction

$$2H_2O_2 \xrightarrow{Fe_2O_3,\, H^+} 2H_2O + O_2$$

The volume of oxygen gas collected is considered as a measure of heterogeneous catalytic activity of the samples.[32-33]

In this work, as seen from Figure 6 and Table 3, the samples F-123 and F-125 showed the least activity for the decomposition of H_2O_2. They also had very low activity in sunlight as the volume of O_2 evolved was almost negligible. The evolution of O_2 from H_2O_2 is assumed to follow Fenton-like process wherein Fe^{2+} is produced insitu from the ferric oxide.

$$Fe_2O_{3(S)} + 4H^+ + H_2O_2 \rightarrow 2Fe^{2+} + 3H_2O + O_2$$

Fe^{2+} then generates further intermediates HO^* and HO_2^* which are responsible for producing O_2.[31] The rate of production of Fe^{2+} would thus govern the rate of O_2 liberation. Further in the photo-Fenton process, the sunlight would

excite an electron into the conduction band. This electron would cause a reduction of the ferric iron from the oxide surface ($e^-_{CB} + Fe^{3+} \rightarrow Fe^{2+}$). Thus the low activity for H_2O_2 decomposition would imply non availability of electrons for the redox process.

The band gap values as obtained from UV-Vis spectra is generally reported to be around (2.10 eV).[32] However, in the present case, the samples showed relatively lower band gap values in the range 1.80-2.08 eV (Table 1). The lower band gap could facilitate the electron-hole pair recombination with the consequent nonavailability of electrons for the Fe^{3+} reduction process. The electron from the conduction band may also be nonavailable by its dissipation of energy through a lattice relaxation process.

Table 3. Catalytic decomposition of hydrogen peroxide in relation to the electrochemical characteristics of the H_2O_2 fuel cell

Catalyst	Phase	H_2O_2 decomposition Vol. of O_2 evolved (mL) Dark	Sunlight	OCP (V)	Current (μA) at 0.4 V	0.2 V	Peak power (μW)
F-121	α-Fe_2O_3	9	0	0.65	1.4	2.4	0.064
F-122	α-Fe_2O_3	19	3.7	0.65	1.4	3.1	0.073
F-123	γ-Fe_2O_3	5	0	0.66	1.4	4.5	0.134
F-125	$\alpha + \gamma$-Fe_2O_3	7	1	0.61	1.5	4.5	0.130
(i) F-125/graphene				-	2.5	8	0.220
(ii) F-125/graphene/hydrazine sulphate nanocomposite				-	86.0	-	1.870

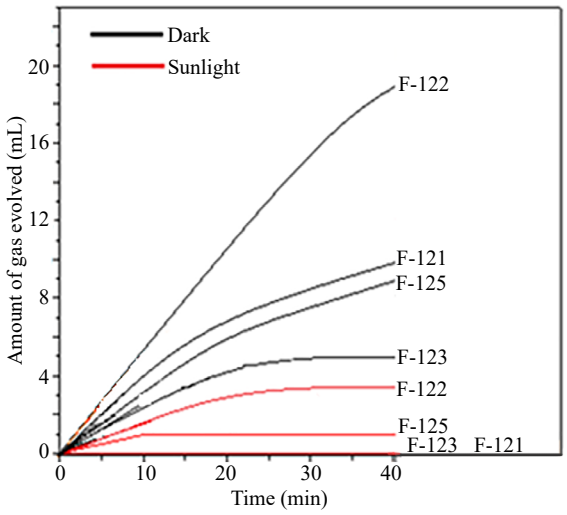

Figure 6. Catalytic decomposition of H_2O_2 on various iron oxides

3.3 *Electrocatalytic activity of iron oxides*

The OCP was determined for a one-compartment fuel cell in a solution of 1 M H_2O_2 + 1 M NaCl. The electrodes were Ag wire and a GCE coated with the sample as a test electrode. Figure 7(b) gives Tafel polarization curves. F-123 and F-125 showed much higher currents than F-121 or F-122. Thus as expected, the (α, γ) mixed-phase oxide which did not favor the catalytic decomposition of H_2O_2, showed higher electrocatalytic activity.

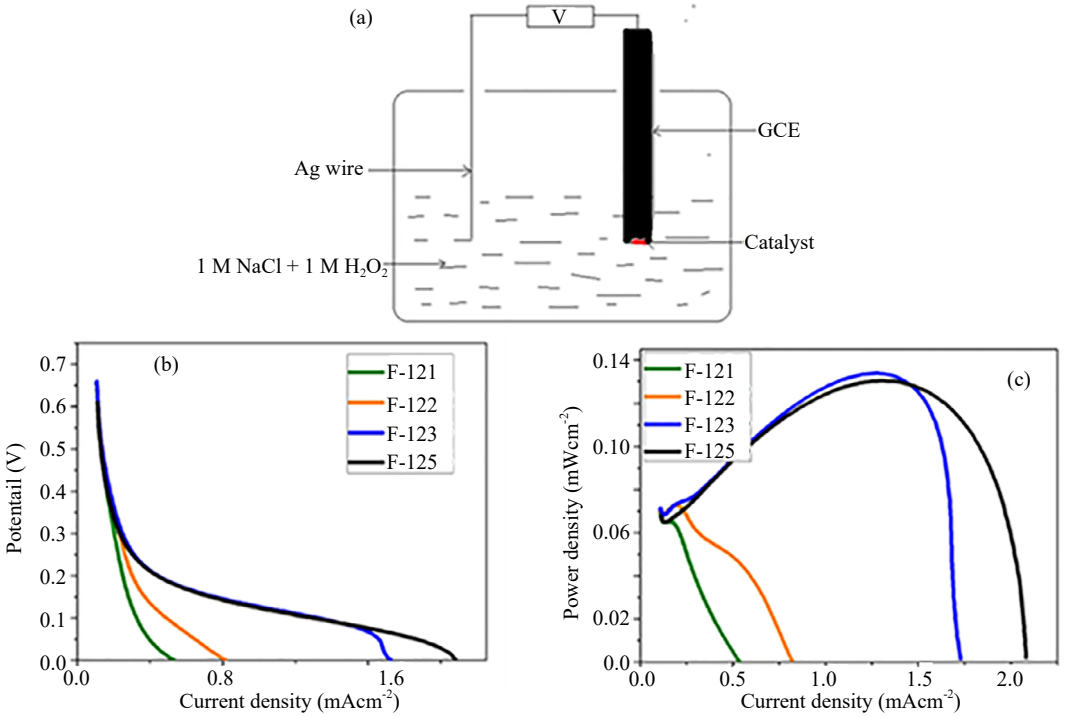

Figure 7. (a) The fuel cell assembly for measuring open circuit potential (b) Tafel polarization plots (c) current-power profiles

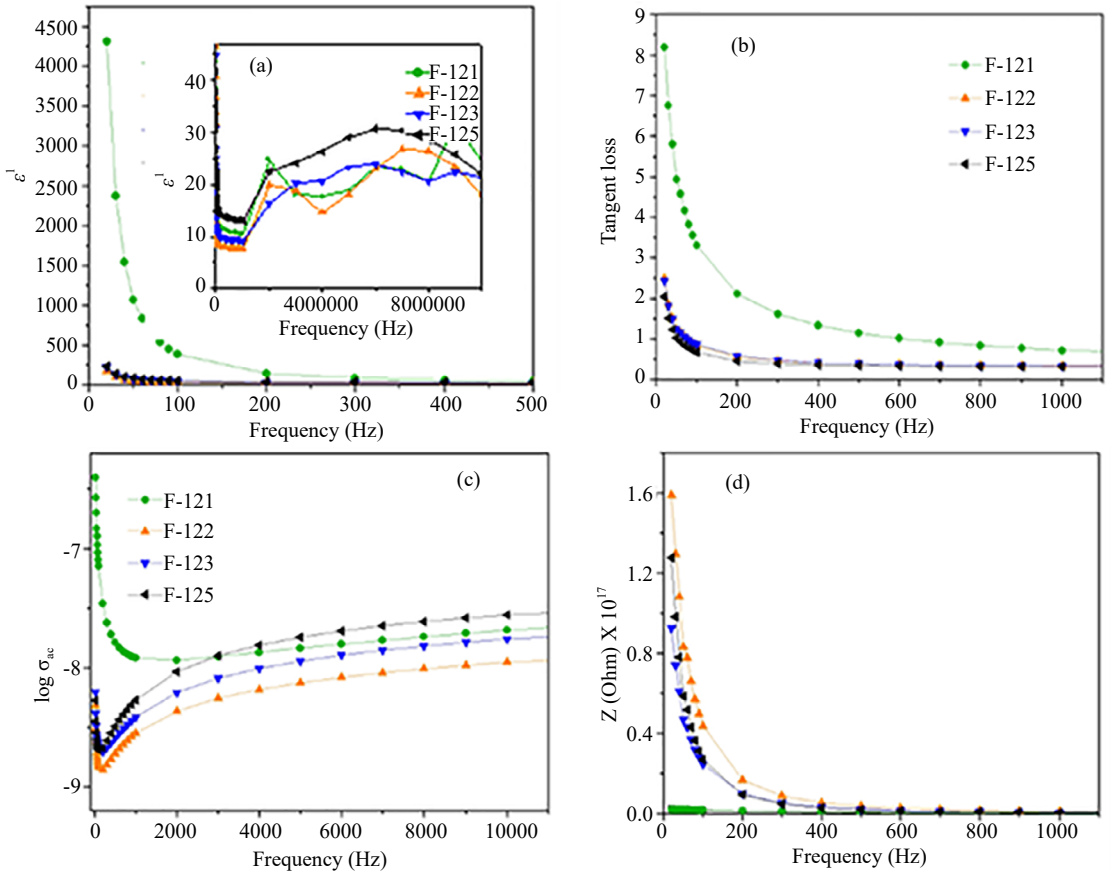

Figure 8. Electrical properties of the synthesized samples (a) Measurements of dielectric constant as a function of ac frequency (b) Variation in the tangent loss (c) Variations in ac electrical conductivity (d) Changes in the impedance with frequency

The hematite samples F-121 and F-122 were more active for catalytic decomposition of H_2O_2. This explains the rapid drop in their potential (Figure 7b). However, in the case of F-123 and F-125, the rate of fall of potential with an increase in current was much slower. These samples particularly F-125, showed a higher dielectric constant (Figure 8).[33-35] This would facilitate stronger adsorption interaction of Fe^{3+}-$O^{2-}\cdots H_2O_2$ and consequent electrocatalytic reduction of H_2O_2. It is known that the iron oxides show a hopping mechanism wherein the electrons from p-orbitals of O^{2-} jump over to Fe^{3+} of the iron oxide lattice. F-125 shows higher electrical conductivity implying that it would facilitate electron transfer to H_2O_2 in the adsorption complex. This would cause facile electrochemical reduction of H_2O_2 in the case of F-125. Also, F-125 had a significantly larger surface area (~ 42 m^2 g^{-1}) that would further facilitate the anchoring of H_2O_2 to the electrocatalyst and facilitate the redox process. Figure 9(a) shows the Tafel plot in the presence of graphene. The composite showed more than double enhancement in activity and higher power output (Figure 9b) due to its improved conductivity pathways.

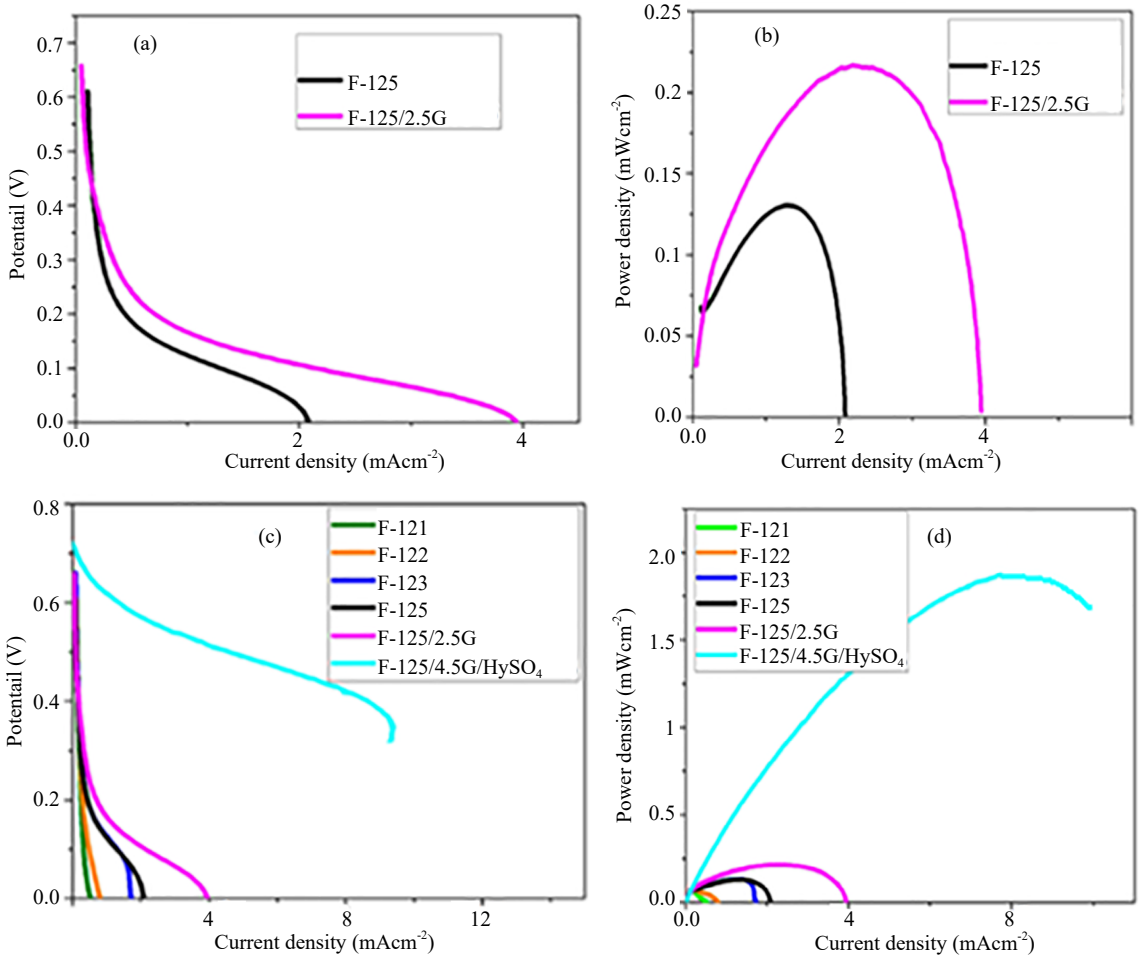

Figure 9. (a) Tafel plots for F-125 and its composite (b) and (d) are power-current profiles. (c) activity of the iron oxide/graphene composite with hydrazine sulphate

Thus, with reference to the Tafel plots in Figure 7(b) and the corresponding values shown in Table 3, it is seen that the potential decreases to 0.4 V when the current output is merely 1.5 units. On the other hand, a high current output of 8.6 mA·cm^{-2} was possible at 0.4 V for the Fe_2O_3-graphene-hydrazine sulphate nanocomposite. It is well known that hydrazine increases the conductivity in graphene by restoring the sp^2 hybridized network.[36] The components of the nanocomposite viz the iron oxide, graphene and hydrazine sulphate collectively facilitate anchoring the H_2O_2 and facilitate the electron transfer pathways for its electrochemical reduction.

4. Conclusions

(i) Several iron oxides were synthesized by calcination of Fe (III) nitrate & urea mixtures in the presence of increasing concentrations of oxalic acid. The increasing use of oxalic acid resulted in the formation of oxides of lower particle size, larger surface area & pore volume, higher dielectric constant and AC conductivity.

(ii) Synthesised iron oxides were investigated for electrocatalytic activity of iron oxides in H_2O_2 fuel cells. They generally showed low activity as evident from rapidly sloping current-voltage profiles.

The electrocatalytic activity followed the order F-125 > F-123 > F-122 > F-121. The activity depends on the surface properties and phase of the iron oxides.

(iii) The activity was enhanced for a composite electrode of F-125 and graphene. An unusually high activity was observed when the iron oxide/graphene composite was further blended with hydrazine sulphate.

Conflict of interest

The authors declare no competing financial interest.

References

[1] Drew, K.; Girishkumar, G.; Vinodgopal, K.; Kamat, P. *J. Phys. Chem. B Lett.* **2005,** *109*, 11851-11857.
[2] Wang, P.; Wang, J.; Fu, L.; Wu, Y. P.; van Ree, T. Metal oxides in fuel cells. *J. Metal Oxides in Energy Technology* **2018,** 17-47.
[3] Zhang, Z.; Liu, J.; Gu, J. J.; Su, L. *Energy and Environment Science* **2014,** *7*, 2535-2558.
[4] Nadzirah, N.; Shaari, N.; Osman, S. J. *Material Science and Technology* **2023,** *39*, 16.
[5] Chorbadzhiyska, E.; Bardarov, I. Graphite metal oxide composites as potential anodic catalysts for microbial fuel cells. *Catalysts* **2020,** *10*, 796.
[6] Schulze, M.; Gülzow, E. *Encyclopedia of Electrochemical Power Sources*; Birtain, 2009.
[7] Wasmus, S.; Kuver, A. Methanol oxidation and direct methanol fuel cells: A selective review. *Electroanalytical Chemistry* **1999,** *461*, 14-31.
[8] Rahimnejad, M.; Adhami, A.; Darvari, S.; Zirepour, A.; Oh, S. E. *Alexendria Engineering Journal* **2015,** *54*, 745-756.
[9] Firouzjaie, H.; Mustain, W. Catalytic advantages, challenges, and priorities in alkaline membrane fuel cells. *ACS Catal* **2020,** *10*, 225-234.
[10] Perumal, R.; Bali, S.; Balakrishnan, M.; Mathur, A. *IECEC-97 Proceedings of the Thirty-Second Intersociety Energy Conversion Engineering Conference*; Honolulu, USA, 1997.
[11] Opakhai, S.; Kuterbekov, K. Metal supported solid oxide fuel cells: A review of recent development and problems. *Energies* **2023,** *16*, 4700.
[12] Zerbinati, O.; Mardan, A.; Richter, M. A direct methanol fuel cell. *J. Chem. Educ*. **2002,** *79*, 829.
[13] Shaegh, S. A. M.; Ehteshami, S. M. M.; Chan, S. H.; Nguyen, N.; Tan, S. *RSC Advances* **2014,** *4*, 37284.
[14] Skrzypkiewicz, M.; L-Radziejewska, I.; Jewulski, J. *Int. J. Hydrogen Energy* **2015,** *40*, 13090-13098.
[15] Zhao, M.; Lv, X.; Jia, Y. *Electrochemistry Communication* **2022,** *142*, 107372.
[16] Yamada, Y.; Yoneda, M.; Fukuzumi, *S. Chem. Eur. J.* **2013,** *19*, 11733-11741.
[17] An, L.; Zhao, T.; Yan, X.; Zhou, X.; Tan, P. The dual role of hydrogen peroxide in fuel cells. *Sci. Bull* **2015,** *60*, 55-64.
[18] Yamada, Y.; Fukunishi, Y.; Yamazaki, S.; Fukuzumi, S. *Chem Comm.* **2010,** *46*, 7334-7336.
[19] Shaegh, S. A. M.; Nguyen, N.; Ehteshami, S. M. M. Chan, S. H. A. *Energy and Env Sci.* **2012,** *5*, 8225-8228.
[20] Shaegh, S. A. M.; Nguyen, N.; Ehteshami, S. M. M.; Chan, S. H. A.; Nguyen, N. T. M.; Tan, S. N. *J. Mater. Chem. A* **2014,** *4*, 1-3.
[21] Oh, T. Design and specifications of direct borohydride-hydrogen peroxide fuel cell system for space missions. *Aerospace Science and Technology* **2016,** *58*, 511-517.
[22] Mazzapioda, L.; Vecchio, C.; Arico, A.; Navarra, M.; Baglio, V. *Catalysts* **2019,** *9*, 1017.
[23] Teja, A.; Koh, P. *Progress in Crystal Growth and Characterisation of Materials* **2009,** *55*, 22-45.

[24] Yu, X.; Kuai, L.; Geng, B. Pt nanoparticles residing in the pores of porous $LaNiO_3$ nanocubes as high efficiency electrocatalyst for direct methanol fuel cells. *Nanoscale* **2012,** *4*, 5738-5743.
[25] Cheng, S. N.; Zhou, J.; Zhang, Z.; Li, S. B.; Ni, J.; Wu, K.; Irvine, J. *Energy Environ. Sci*. **2021,** *14*, 6287-6319.
[26] Marcano, D. C.; Kosynkin, D. V.; Berlin, J. M.; Sinitskii, A.; Sun, Z. Z.; Slesarev, A.; Alemany, L. B.; Lu, W.; Tour, J. M. *ACS Nano* **2010,** *4*(8), 4806-4814.
[27] Inamdar, S.; Ingole, P.; Haram, S. Determination of band structure parameters and the quasi particle gap of CdSe quantum dots by quantum dots by cyclic voltametry. *Chem. Phys. Chem*. **2008,** *9*, 2574-2579.
[28] Malina, O.; Tucek, J.; Jakubec, P.; Kaslik, J.; Medrik, I.; Tokoro, H. *RSC Adv.* **2015,** *5*, 49719.
[29] Fukuzumi, S. Artificial photosynthesis for production of hydrogen peroxide and its fuel cells. *Biochimica et Biophysica Acta (BBA)-Bioenergetics* **2016,** *1857*, 604-611.
[30] Williamson, G.; Hall, W. X-ray line broadening from filed aluminium and wolfram. *Acta. Metall.* **1953,** *1*, 22.
[31] Dolabella, S.; Borzi, A.; Dommann, A.; Neels, A. *Wiley Online Library* **2021,** *6*, 2100932.
[32] Shete, M.; Fernande, J. A simple solid state method to synthesis nanosized ferromagnetic α-Fe_2O_3 with enhanced photocatalytic activity in sunlight. *Bull. Mater. Sci.* **2019,** *42*, 254.
[33] Shete, M. D.; Fernandes, J. B. A simple one step solid state synthesis of nanocrystalline ferromagnetic α-Fe_2O_3 with high surface area and catalytic activity. *Mat. Chem. and Phy.* **2015,** *165*, 113-118.
[34] Onari, S.; Arai, T.; Kudo, K. Infra red active vibrations and dielectric dispersion in α-Fe_2O_3. *Phys. Rev. B* **1977,** *16*, 1717-1721.
[35] Wang, C.; Liu, H.; Sun, Z. M. Heterogenous photo-fenton reaction catalysed by nanosized iron oxides for water treatment. *Int. J. Photoenergy* **2012,** 2012.
[36] Matsumoto, Y.; Sato, E. Electrocatalytic properties of transition metal oxides for oxygen evolution reaction. *Mat. Chem. and Phy*. **1986,** *14*, 397-426.